Design Optimization of a Spoke Type Axial-Flux PM Machine for In-wheel Drive Operation

Zhou Shi, Xiaodong Sun, *Senior Member, IEEE*, Zebin Yang, Yingfeng Cai, *Senior Member, IEEE*, Gang Lei, *Senior Member, IEEE*, Jianguo Zhu, *Senior Member, IEEE*, and Christopher H. T. LEE, *Senior Member, IEEE*,

***Abstract*—Axial flux machines have huge potential in direct-drive operations such as In-wheel drive operation due to the characteristics of high torque density and short axial length. However, the design optimization of axial flux machines was limited by the lack of accuracy magnetic circuit model. In this paper, a spoke-type axial-flux permanent magnet synchronous machine (Spoke-type AFPMSM) is designed and an efficient optimization method for axial flux structure is proposed. The proposed optimization method improves the efficiency of the optimization design by using a 2-D equivalent finite element model and multilevel optimization strategy. The parameters without end effects will be optimized by a 2-D equivalent model and the parameters with end effects will be optimized by a 3-D model. In this way, the number of finite element nodes required for optimization calculation can be minimized. Besides, the multilevel strategy and response surface optimization method are also adopted to further improve the efficiency of the optimization. The proposed method improved the cost, efficiency, and torque of the AFPMSM significantly, and some other constraints are also considered in the optimization progress. Finally, experimental results based on a prototype are provided to validate the performance of the proposed AFPMSM. The proposed method can be applied for other design optimization of axial flux operations.**

***Index Terms*—Multi-objective optimization, Axial Flux permanent magnet synchronous machine (AFPMSM), Finite element analysis, Response surface optimization.**

I. INTRODUCTION

In recent years, electric vehicles (EVs) replaced the position of fuel vehicles in the passenger car market, and electric drive technology has gradually become the mainstream vehicle drive technology [1-3]. Though centralized drive mode is adopted in most EV drive systems, distributed drives still have huge potential due to the distributed drive capability, no transmission system, and free space for vehicle body design [4-8]. Centralized drive machines can enhance power density by adopting higher rotational speeds. Instead, the speed range of the machine and the speed of the in-wheel machine is decided by the vehicle speed and tire size. Therefore, axial flux machines (AFMs) are the most suitable machine type for in-wheel drive applications due to its characteristic of axial compactness, high torque-to-volume ratio, and high material utilization [9-11]. According to the number of air gaps, axial flux machines can be divided into single-side AFMs, double-side AFMs, and multi-disc AFMs as shown in Fig.1. In these structures double-side AFMs with two rotors and one stator also called two outer rotors and one stator structure (TORUS) as shown in Fig.1(c) is the most popular structure for in-wheel drive application as it has short radial dimensions and balanced radial forces. According to the machine type the AFMs can be divided into axial-flux permanent magnet synchronous machines (AFPMSMs), axial-flux switched reluctance machines, axial-flux induction machines, and axial flux-switching permanent magnet machines [12-14]. Among these types of AFMs, spoke-type AFPMSMs can provide the highest torque density by adopting a spoke-type structure and using permanent magnet material with high remanence [15].

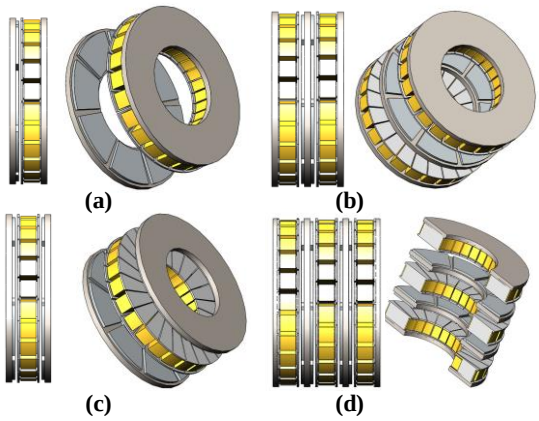

Fig. 1. AFM with different structures. (a) Single gap AFM, (b) Two gaps outer rotor AFM, (c) Two gaps inner rotor AFM, (d) Multi gaps AFM.

There are several types of analysis methods adopted in the study of AFMs. 3-D equivalent magnetic network (EMN) modeling is adopted in the study of an axial-flux hybrid-excitation machine [16, 17]. Regarding the existing EMN modeling method that cannot meet the special structure of the AFMs, a 3-D EMN modeling method was proposed compared with the 3-D finite element model (3D-FEM) the proposed 3-D EMN can save computation time by 95% with an error of about 5% [18]. In [19], the field reconstruction method (FRM) was used in the research for an AFPMSM, in which a virtual air gap concept was proposed to deal with the parallel slot effect as well as the overhang effect. Compared with 3D-FEM, FRM can save computation time by 80%. In [20], an airgap magnetic field distribution analytical model was proposed to deal with AFPM

machines with various types of misalignments. Compared with the 3D finite element model, these models save the calculation time under the condition of sacrificing some accuracy. In this study, to reduce the calculation time of the optimal design of the AFPMSM, the Quasi-3D FEM model will be used for some parameters which have no significant end effects.

Apart from the simulation model, the computation efficiency of design optimization progress also depends on the optimization model structure, the number of parameters to be optimized, and optimization algorithms [21-23]. Multilevel optimization strategy and approximate models are the most popular methods to improve computation efficiency. In [24] multilevel optimization method is used to control the number of parameters to be optimized in a reasonable range, in which the iterative time was saved compared with global optimization and satisfied optimized results were achieved by this method. Response surface optimization is another method to improve optimization efficiency. Approximate models including the response surface model (RSM), Kriging model, radial basis function (RBF) model, and artificial neural network (ANN) model are adopted to fit the inputs and outputs of an electromagnetic system to reduce the FEMs to be calculated in the optimized progress [25-27]. In this study, both methods will be adopted to improve the efficiency of the optimization combined with the use of suitable simulation models.

This paper aims to design an AFPMSM for an in-wheel drive application. Besides, an optimization method for AFMs that can improve optimization efficiency by adopting a multilevel optimization strategy and approximate models is proposed in this paper. In multilevel optimization, the parameters to be optimized are assigned to different optimization levels, in each optimization level only 3-4 parameters need to be optimized and others are fixed. The remainder of the paper is organized as follows. In Section II, to meet the requirements of in-wheel drive operations a novel spoke-type AFPMSM with a trapezoidal permanent magnet is proposed and the initial design of the prototype is carried out based on the collected driving cycle. In Section III, to achieve efficient optimization of the proposed AFPMSM, the optimization method consists of a multilevel strategy, Quasi-3D FEM model, and Kriging model are proposed which can improve the efficiency of the optimization progress significantly. And NSGA II is adopted as the multi-objective optimization algorithm in multilevel optimization. Section IV shows the experimental results of the spoke-type AFPMSM prototype and the comparisons between simulated and measured results, followed by the conclusion.

II. Machine Structure and Initial Design

In this section, the topology choice and structure of the novel AFPMSMs will be introduced first. Then the design principles and initial design of the spoke-type AFPMSMs for EVs application will be introduced. Finally, the parametric finite element model will be established, and finite element analysis will be carried out to verify the electromagnetic performance of the initial design of the proposed Spoke-type AFPMSM.

For in-wheel drive operations, the torque density is the most important indicator. Compared with single-side structures double-side AFMs can provide higher torque density and balance the magnetic force between the rotor and stator. Compared with the multi-disc structure, the double-side AFMs are much more friendly to thermal design and have a simple mechanical structure. Besides, double-side AFMs have better tolerance performance under tilt operations. Therefore double-side AFMs structure is much more suitable for in-wheel drive operations. In this study, AFM with two rotors and one stator structure is adopted.

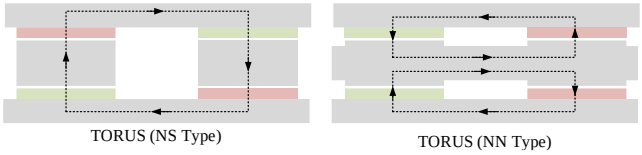

Fig. 2. TOURS type AFPMSM. (a)TOURS NS type, (b) TOURS NN type.

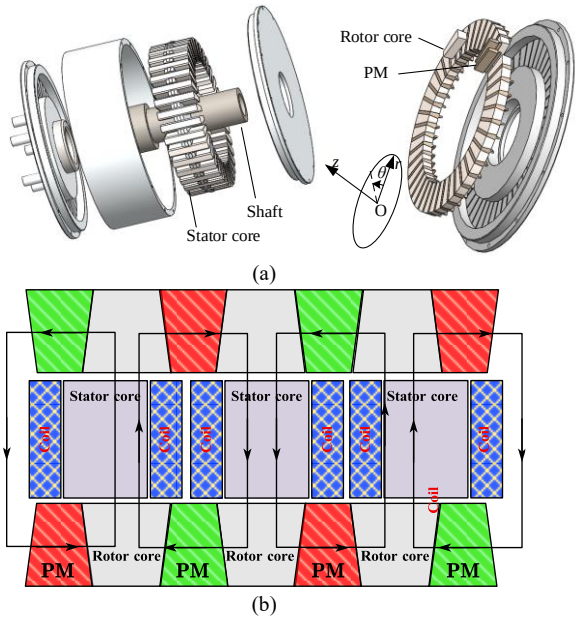

Fig. 3. Topology and magnetic circuit of the proposed Spoke-type AFPMSM. (a) Mechanical topology, (b) Magnetic circuit topology.

For TORUS machines, according to the difference in magnetic flux path, TORUS machines can be further divided into TORUS-NN type and TORUS-NS type as shown in Fig. 2. Compared with the TORUS-NS structure, the TORUS-NN structure requires a certain number of stator iron lines to provide tangential magnetic circuits for the magnetic circuits on both sides, which increases the axial thickness of the stator on the one hand and increases the magnetic resistance on the other hand which will lead to the increase of core loss. In addition, changing the magnetic circuit structure has high requirements on the 3-D magnetic conductivity of the core material, while the TORUS-NS structure only requires the magnetic permeability of the stator in the *r*-*z* plane. There is no magnetic permeability requirement in the θ-*r* plane. Therefore TORUS-NN structure has lower core loss and has more optional core materials.

In the aspect of PMs structure, the rotor with spoke type PMs

structure can enhance the permanent magnet flux by increasing the rotor axial length while the airgap permanent magnet flux surface mount PMs structure is limited by the permanent magnet remanence. Therefore, AFPMSMs with spoke-type PMs structure can provide much higher airgap flux density which contributes to a higher torque density.

Taking all these aspects into consideration the topology of the AFPMSM designed for this study is shown in Fig. 3 (a), and the magnetic circuit structure of the machine is shown in Fig. 3(b). Differently from the ordinary spoke-type PMs structure, a trapezoid section PM is adopted in this design instead of a rectangular section PM which can improve the torque performance of the machine. And the specific dimension of the machine will be discussed in the optimization progress.

B. Initial Design

For centralized drive machine design, the power density can be improved by increasing the max rotation speed and changing the transmission ratio to match the machine rotation speed to the vehicle speed.

Instead, for the in-wheel direct drive machine for vehicles, its design is significantly different. First, the rotation speed is demanded by the driving cycle and tyres size directly. Second, the external dimension of the hub machine is limited to a much thinner machine structure due to the hub space.

In this study, the hub drive machine is designed as an experimental vehicle for road condition acquisition. The driving cycle of the vehicle usually used is collected on a test vehicle and the working point of the machine is calculated based on the driving cycle, vehicle dynamic model, and vehicle parameters. The machine working points are shown in Fig.4.

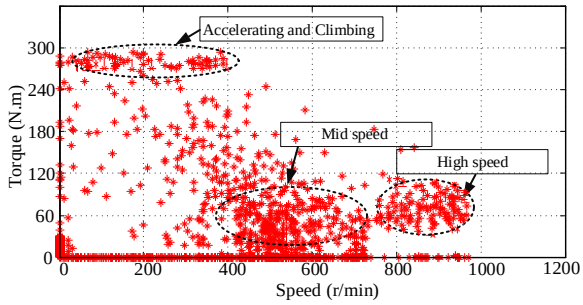

Fig. 4. Machine working points in one driving cycle.

As shown in Fig.4, under accelerating and climbing working conditions the maximum torque should reach 280Nm. Mid-speed operation is the most frequent operation, the machine needs to maintain high efficiency during this operation. The high-speed operation can reach over 1000 r/min and keep the torque over 90 Nm.

Under the condition of ignoring leakage inductance and resistance, the power dimension of the machine can be expressed as (1):

$$P_{\text{out}} = \eta \frac{m}{T} \int_0^T e(t) \cdot i(t) dt = m K_p \eta E_{pk} I_{pk} \qquad (1)$$

where η is the mechanical efficiency, m is the number of phases, T is the electrical periodic of the machine, E_{pk} and I_{pk} are the peaks of phase electromotive force (EMF) and current, respectively, and K_{p} is the electrical power waveform factor. For the EV drive machine, the maximum constant torque operating point can be chosen as the basic design point. Therefore, in this design, the AFPMSM should reach 280Nm at 400r/min under the E_{pk} and I_{pk} condition. For the axial flux machine, the sizing equation can be expressed as:

$$P_{\text{out}} = \frac{1}{1+K_\phi} m K_e K_i K_p K_L \eta \cdot B_g A \frac{f}{P} (1-k_1^2) \left(\frac{1+k_1}{2}\right) D_o^2 L_e \qquad (2)$$

Where P_{out} is the output power, A is the electric load, K_Φ is the electric load rate, L_e is the axial length, m is the phase number, K_e and K_i are EMF the current waveform factor respectively, K_p is the voltage waveform power factor, K_L is the aspect ratio coefficient of specific machine structure, η is the mechanical efficiency, B_{g} is the air gap flux density, A is the current load, f is the frequency, P is the rotor pole pair, $k_1=D_i/D_{\text{o}}$ is the split ratio, D_{o} is the outer diameter, and Le is the effective axial length.

Table I.
Key Design Parameter of the Proposed AFPMSM

Parameters	Symbol	Values	Unit
DC voltage	U_{dc}	300	V
Max Phase current (Peak)	I_{pk}	75	A
Rated speed		600	r/min
Maximum speed		1200	r/min
Maximum power	P_{max}	15	kW
Maximum current density	J_{max}	9.5	A/mm^2
Slot filling factor	k_f	0.55	
Stator slot number	N_s	36	
PM pole pairs	P	21	
Phase number	m	3	
Outer diameter	Do	260	mm
Axial length	L_e	100	mm
Split ratio	k_1	0.7	

Compared with the internal PM machine more rotor pole pair is needed for AFPMSMs to reduce the flux of each rotor pole as the increasing of pole flux will lead to the increase of rotor thickness. In the aspect of winding structure fractional slot concentrated winding is the best choice for AFPMSMs as it can reduce the length of end winding and is friendly to modular production which is necessary for AFPMSMs manufacture. Besides, due to the lack of a transmission system the electrical frequency is determined by the vehicle speed directly, the choice of rotor pole number should consider the speed range and tire size to make sure the machine's high-efficiency range matches the high-frequency operating range. Besides, the rotor pole number should not be too high to avoid excessive core loss. Based on the above sizing equations and design criteria, the initial design of the AFPMSM is shown in Table I. In this design, passive cooling is adopted, resulting in a low current density. The maximum transient current density is 9.5A/mm^2, and under continuous high-speed operation the maximum allowed current density is 6 A/mm^2. The temperature rise of the machine under different conditions has been simulated and

verified to ensure it is within a reasonable range.

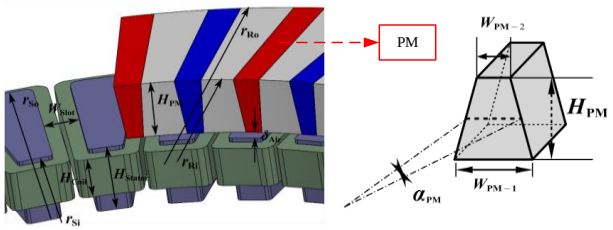

Fig. 5. Parameterized model of the proposed Spoke-type AFPMSM.

C. Parametric Finite Element Model

The topology of the proposed AFPMSM is shown in Fig.5 and the parameters of the initial design of the AFPMSM are given in Table II. In this design, a trapezoidal shape PM structure is adopted which can increase the core area on the air gap side, which is beneficial for improving the pole arc coefficient.

A thicker permanent magnet away from the air gap side can improve the anti-demagnetization ability of the permanent magnet and make the magnetic leakage circuit side of the permanent magnet longer which can reduce the magnetic leakage.

To improve the calculation efficiency of the FEM, a 1/12 3D-FEM was established to analyze the electromagnetic performance which takes both symmetry and periodicity into consideration.

Some basic electromagnetic performance of the initial design is analyzed to confirm that the initial design can fit the design requirements.

As shown in Fig. 6(a), the peak value air gap flux density can reach 1.2T which is higher than the air gap flux density of other AFPMSMs with surface-mounted PM structure. There is a significant flux leakage at the inner and outer sides of the rotor resulting in a relatively low air gap flux density. The cogging torque of the machine is less than 6 Nm as shown in Fig. 6(b).

Fig. 6(c) shows the no-load-back EMF at 600r/min (210Hz), and the harmonic frequency of the back EMF are given in Fig. 6(d) the amplitude of the fundamental wave is 164 V, and the third harmonic component is 6.8 V, with the highest amplitude of other higher harmonics being 0.22 V.

As shown in Fig. 6(f), when the Phase current (RMS) reaches 50 A the torque of the proposed can meet the maximum torque requirements. In analysis, the torque can reach over 400 Nm while in real design the maximum torque cannot reach such value due to the limit of current density. The torque ripple is less than 3.9 % under the condition of 6 A/mm^2 current density as shown in Fig. 6(e).

To verify There are several challenges Fig. 7(a) shows the lowest magnetic flux density distribution of a PM during one electrical period. As shown in Fig.7 (a) the magnetic flux density of the part which is close to the air gap is the lowest. And the demagnetization ratio distribution of this part is the highest. In this study, the demagnetization ratio (D_{mag}%) is defined as:

$$D_{mag}\% = \frac{R}{B_r} * 100\% \quad (3)$$

where B_r is the residual magnetic strength of permanent magnets and R is the residual magnetic strength after demagnetization.

Table II.
Geometric Parameters of the Proposed Spoke-type AFPMSM.

Var.	Sym.	Initial value	Remarks
Slot number	Q	36	
Pole pair number	P	21	
Rotor outer radius	r_{Ro}	mm	
Rotor inner radius	r_{Ri}	mm	
Split ratio	λ	/	r_{Ri}/r_{Ro}
Rotor radius	r_R	mm	$r_{Ri} < r_R < r_{Ro}$
Height of the PM	H_{PM}	mm	
Polar arc coefficient	k_{PM}	/	
Polar arc angle	α_{PM}	/	$\alpha_{PM}=\pi/P*k_{PM}$
PM skew rate	k_{PM1}	0	$0 < k_{PM1} < 1$
PM pole arc correction factor	k_{PM2}	0	$0 < k_{PM2} < 1$
PM mid-width	W_{PM}	mm	$W_{PM}=\alpha_{PM}*r*[1-(r-r_{ri})/(r_{ro}-r_{ri})*k_{PM2}]$
PM upper width	W_{PM-1}	mm	$W_{PM-1}=W_{PM}*(1+k_{PM1})$
PM underside width	W_{PM-2}	mm	$W_{PM-2}=W_{PM}*(1-k_{PM1})$
Stator outer radius	r_{So}	mm	$r_{so}=r_{ro}$
Stator inner radius	r_{Si}	mm	$r_{si}=r_{ri}$
Stator Height	H_{Stator}	mm	
Coil Height	H_{Coil}	mm	$H_{Coil}=H_{Stator}$-2mm
Slot width	W_{coil}	mm	
Airgap length	δ_{Air}	mm	
Stator inner lip	Lip_{in}	0 mm	$Lip_{in}= r_{So}- r_{Ro}$
Stator outer lip	Lip_{out}	0 mm	$Lip_{out}= r_{Si}- r_{Ri}$

The demagnetization ratio will be influenced by material and temperature, in this study the PM material is N48SH, and the temperature adopt for the analysis in Fig. 7(b) is 120 ℃. Besides, the torque wave before and after demagnetization under different temperatures are also analyzed and the results are given in Fig. 7(c). As shown in Fig. 7(c) when the temperature is lower than 120 ℃ the influence of demagnetization on the torque is slight, however when the temperature reaches 150 ℃ the influence of demagnetization on the torque is unacceptable. In this design, passive cooling is used. The maximum current density is 9.5A/mm^2 under 200 r/min, and 6 A/mm^2 under 1000 r/min. The temperature rise results of this machine under the two conditions are presented in Fig 8. As shown in Fig 8(a), under the speed of 200 r/min and current density of 9.5 A/mm^2, the winding temperature can reach 95 ℃ and the PMs temperature is lower than 80 ℃ after 600 s continuous operation. As shown in Fig 8(b), under the speed of 1000 r/min and current density of 6 A/mm^2, the winding temperature can reach 97 ℃ and the PMs temperature can reach 95 ℃ after 1800 s continuous operation. In summary, the demagnetization risk of permanent magnets is relatively low.

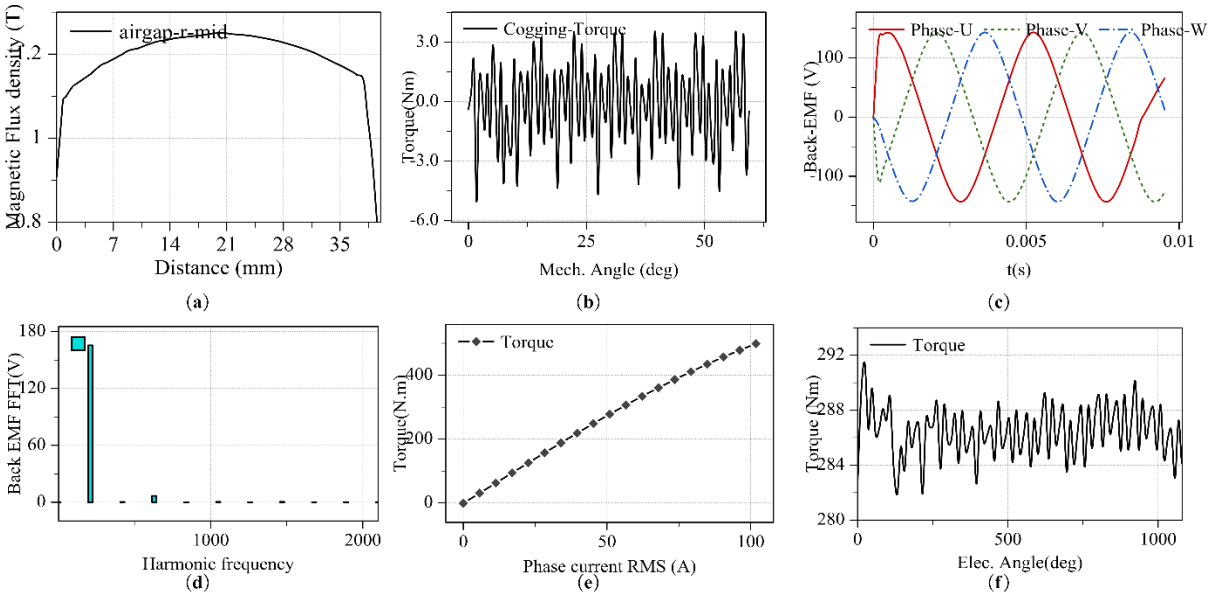

Fig. 6. FEM results of the proposed Spoke-type AFPMSM.(a) Airgap flux density, (b) cogging torque, (c) back-EMF@400 r/min, (d) back-EMF FFT, (e) torque waveform, and (f) torque current curve.

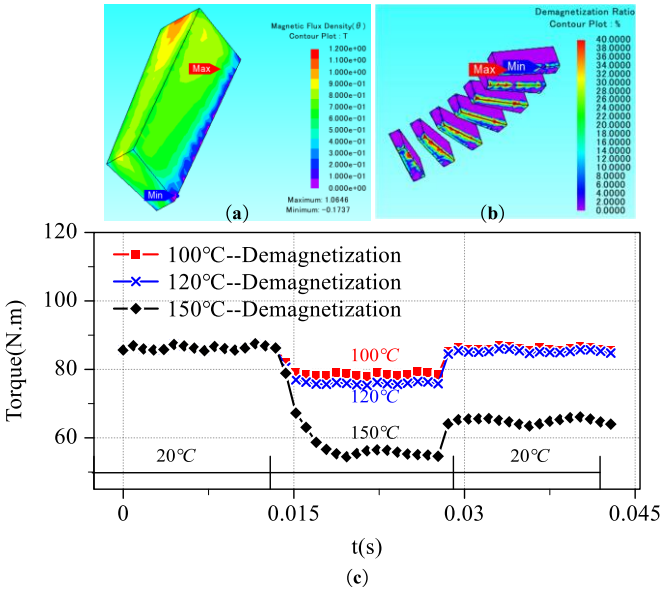

Fig. 7. (a) Magnetic flux density distribution, (b) demagnetization ratio distribution, and (c) torque wave under different temperature demagnetization.

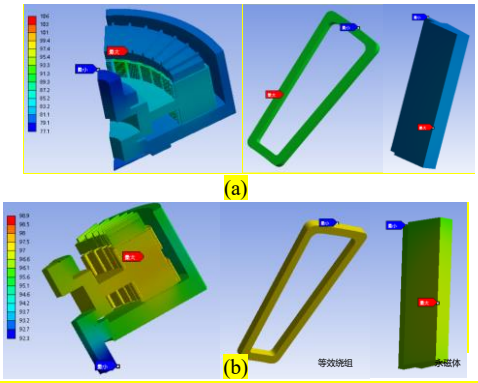

Fig. 8. Temperature rise (a) 200r/min, 9.5A/mm^2, 600s (b) 1000 r/min, 6 A/mm^2, 1800s.

III. Multi-Objective Optimization Based on Multilevel Strategy

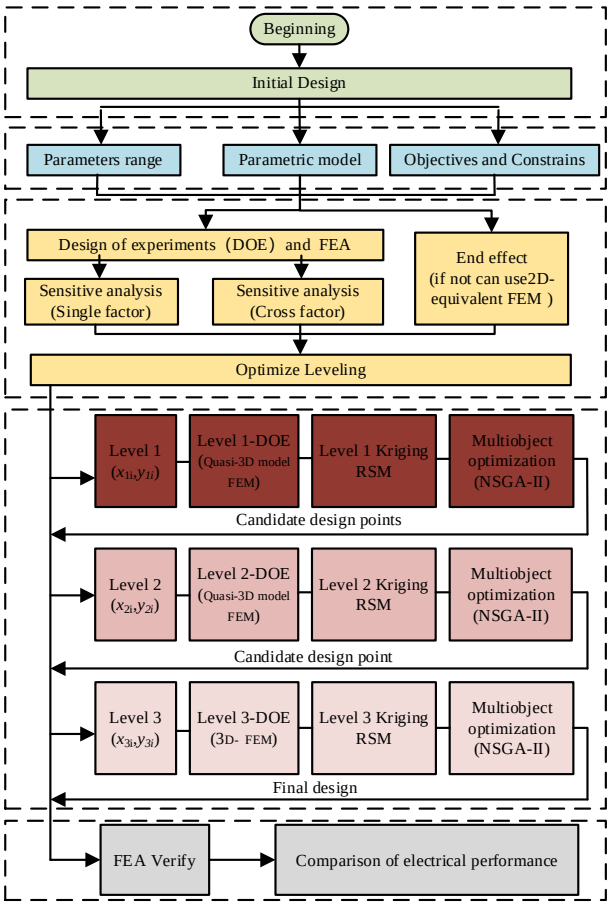

Fig. 9. Multilevel optimization flowchart for proposed AFPMSM.

There are several challenges in the multi-objective

optimization of AFMs. First, AFMs require 3-D finite element analysis (FEA), which increased computation time significantly. Second, multi-objective optimization with several free parameters needs to search the optimal design in a larger design space, which will increase the FE models that need to be calculated. Therefore, a multi-objective optimization method based on a multilevel strategy and Quasi-3D FEM was proposed in this study.

Fig. 9 shows an optimization framework for the proposed AFPMSM based on the proposed multilevel optimization strategy. The initial design parametric model and basic performance analysis have been defined in Section II. Sensitivity analysis including correlation coefficient and cross-factor variance analysis will be carried out based on the orthogonal design of experiments. The variables will be levelled based on the sensitivity analysis results and model types. Then, all the variables will be sequentially optimized in three levels multi-objective optimization. In each multi-objective optimization level, the Kriging model will be adopted to construct response surfaces to reduce the models to be analyzed and NSGA-II will be adopted to optimize.

A. Optimization Objectives and Constraints

For an EV drive machine, dynamic performance, cost, and efficiency are the most important evaluation indicator. Therefore, in this optimization, three objectives have been chosen for the multi-optimization containing the maximum torque ($T_{\max}$), material costs (*Costs*), and driving cycle weighted efficiency ($Effi_{cycle}$). Here the maximum torque refers to the average torque under the maximum allowed current density of 9.5 A/mm^2. In the calculation of material costs only take the mass of materials including magnets, steel, and copper into consideration and processing costs are neglected. The driving cycle weighted efficiency is calculated by weighting the efficiency of different operating conditions and frequencies in the driving cycle.

Table III.
Optimization Parameters Objectives and Constraints of the AFPMSM

Variable		
Name	Symbol	Range
Split ratio	k_1	0.6-0.8
Slot width	W_{coil}	6 mm-8 mm
Height of the PM	h_{PM}	11 mm-16 mm
Polar arc coefficient	k_{PM}	0.3-0.5
PM skew rate	k_{PM1}	0.1-0.25
PM pole arc correction factor	k_{PM2}	0-1
Stator inner lip	Lip_{in}	0 mm-3 mm
Stator outer lip	Lip_{out}	0 mm-3 mm
Objectives and constraints		
Maximum torque	T_{max}	> 250 Nm
Torque ripple	T_{rip}%	< 6%
Driving cycle efficiency	$Effi_{cycle}$%	> 90%
Material cost	*Cost*	< 1000 CNY
Demagnetization torque loss (100℃)	$T_{demgloss}$‰	< 6‰

Aside from the objectives, some constraints are necessary for the optimization to limit the optimization boundaries and restrain some other performance. To reduce the invalid cases calculated in the optimization progress some boundaries need to be set for the optimization objectives. Besides, the limit of torque ripple and torque loss caused by the demagnetization is also necessary. All the parameters to be optimized, objectives and constraints are listed in Table III. In Table III The maximum torque (T_{max}) is simulated under 9.5 A/mm^2 at 400 r/min, the torque ripple (T_{rip}%) is simulated under 6 A/mm^2 at 400 r/min, the driving cycle efficiency ($Effi_{cycle}$%) is the comprehensive efficiency of all work points shown in Fig. 4 based on DC voltage 300 V and MTPA control strategy.

B. Quasi 3D Model and Leveled Strategy

Quasi-3D FEM model

If the 3D FEM is adopted in the whole optimization process, it will consume a large amount of calculation time. There are 8 parameters to be optimized as listed in Table III, except stator inner lip and stator outer lip have obvious end effects, the other 6 parameters only have effects on the flux distribution along the θ direction and z direction. Therefore, quasi-3D FEM can be adopted in the optimization of these parameters.

When ignoring the end effects the flux is only distributed along the θ direction and z direction the quasi-3D FEM can be adopted to replace the 3D FEM by dividing the axial flux machine into several 2D linear machines as shown in Fig. 10. When the axial flux machine was divided into several rings the difference in flux density in radial length can be ignored and the flux in mid radium of each ring can be recognized as the flux density of the 2D cross-section of the equivalent linear machine and $(r_{ro}\text{-}r_{ri})/N$ is equal to the core stack length of the linear machine. The torque can be expressed as follows:

$$\begin{aligned} T &= 2N_{nuit} \times \sum_{i=1}^{j} T_i \\ T_i &= F_i \times R_i \end{aligned} \tag{4}$$

where N_{unit} is the number of radial segments; i is the order of the sections; j is the number of the linear machine used to create the quasi-3D model; F_i and R_i are the force and force arm of the i section; T_i is the equivalent torque of the i section.

Taking the calculation model into consideration the 8 parameters can be divided into two categories. The stator inner lip and stator outer lip can only be calculated in 3D FEM. If the other 6 parameters are optimized in one optimization level the complexity of optimization is still relatively high. To further reduce the computation cost, these six parameters need to be divided into two different optimization levels according to sensitive analysis.

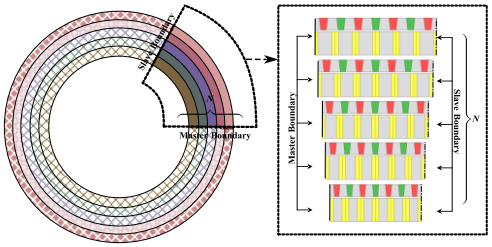

Fig. 10. Quasi-3D FEM of the AFPMSM.

The 1/12 3D FEM need over 300,000 nodes and the quasi-3D FEM with 5 slices only needs about 60000 nodes, which means the calculation cost saved by at least 80%.

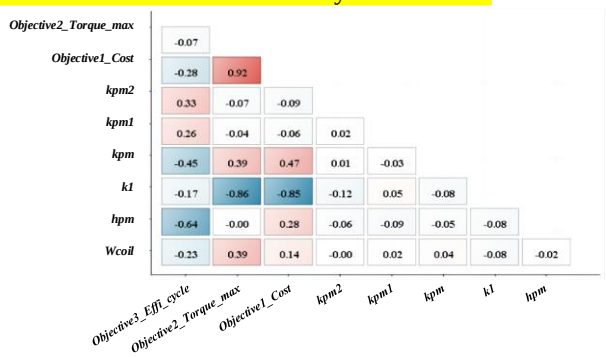

Fig. 11. The Pearson correlation coefficient of the design parameters to the optimization objectives.

Correlation coefficient and Cross-factor variance analysis

To show the linear relationship between the design parameters and the objectives, the Person correlation coefficient is adopted as the sensitivity analysis method in this study which can be given by:

$$\rho_{X_i,Y_i} = \frac{N\sum X_i Y_i - \sum X_i \sum Y_i}{\sqrt{N\sum X_i^2 - (\sum X_i)^2}\sqrt{N\sum Y_i^2 - (\sum Y_i)^2}} \quad (5)$$

where N is the sample size; Y_i is the i-th optimization objective, X_i is the design parameters, and N is the sample size. The results of the Person correlation coefficient between all the design parameters and the objectives are given in Fig.11. As shown, the parameters k_1, h_{pm}, and k_{pm} have relatively high Pearson correlation coefficients, which should be optimized preferentially in multilevel optimization.

In single parameter sensitive analysis, the influence of coherence between parameters will be ignored. Therefore, the cross-factor variance analysis and ***F***-test will be adopted two show the correlation effects. The cross-factor variance and ***F***-test can be given by:

$$s_k^2 = \frac{U_k}{a_k - 1} \qquad s_e^2 = \frac{Q}{\prod_{k=1}^{k}(a_k - 1)} \quad (6)$$

$$F_k = \frac{s_k^2}{s_e^2} \quad (7)$$

where s_k^2 is the variance of the k-th column element, s_e^2 is the variance of random error, Q is the square of deviance, F_k is the ***F***-test result of k-th column element, and (a_k-1) is the degree of freedom of k-th column element.

Table IV.
Cross-Factors with Significant Influence on the Optimization Objectives

Objectives	*Cost*	T_{max}	$Effi_{cycle}$%
Cross factors	(k_{PM}, k_{PM1}) (k_{PM1}, k_{PM2})	(W_{coil}; h_{PM}) (k_1; k_{PM})	(k_{PM}; k_{PM1}) (k_{PM1}; k_{PM2}) (k_{PM}; k_{PM2})

Finally, F-test will be taken to select the cross-factors which are significant to the optimization objectives. The screening criteria are as follows:

$$F_k \geq F_{0.05,\,(a_k-1,\,a_e-1)} \quad (8)$$

where (a_e-1) is the degree of freedom of the random error. In order to study the interaction of these design parameters, the interaction F_k of parameters is carried out. The cross factors which satisfy (4) are listed in Table IV. Take k_{PM1}, k_{PM2} as examples, these two parameters have low Pearson correlation coefficients, while when combined with k_{PM} these two parameters will have a significant influence on several objectives. Therefore, it is suggested to optimize the parameters in the same cross factor with significant influence at the same optimization level.

Levelled optimization

Taking the analysis model, correlation coefficient, and cross-factor variance analysis into consideration, the optimization task can be divided into three levels. The parameters to be optimized, objectives and constraints of different optimization levels are listed in Table V. Parameters k_1, W_{coil}, and h_{PM} are optimized in the first level as they have high correlation coefficients, and maximum torque, material costs, and driving cycle weighted efficiency are all set as the objectives in this level. In second-level optimization k_{PM}, k_{PM1}, k_{PM2} are optimized as their correlation coefficient are relatively low than the parameters in the first level and they have significant cross-factors. In second-level optimization, high-temperature demagnetization torque loss $T_{demgloss}$‰ will be set as the constraint which can be defined as:

$$T_{demglos}‰ = (T_{initial} - T_{demg@120\,℃}) * 1000‰ \quad (9)$$

where $T_{initial}$ is the torque before high-temperature demagnetization $T_{demg@120℃}$ is the torque after high-temperature demagnetization (120℃). In third-level optimization, the stator inner lip (Lip_{in}) and stator outer lip (Lip_{out}) will be optimized and cannot be calculated by the Quasi-3D FEM model. The stator inner lip and stator outer lip are the parameters to describe the radius difference between the stator and rotor. By adopting a different stator and rotor radius the edge leakage of the axial flux machine can be reduced and the manufacturing costs can be saved.

C. Multi-objective Optimization based on the Kriging RSM Model and NSGA II

A multi-objective optimization method based on the Kriging model and NSGA II is adopted for all three levels of multi-objective optimization. NSGA-II is an evolutionary algorithm developed as an answer to the shortcomings of early evolutionary algorithms, which lacked elitism and used a sharing parameter in order to sustain a diverse Pareto set [28, 29].

Take first-level optimization as an example, three parameters need to be optimized. Assuming that the resolution of each parameter within the optimization range is 100, we need to calculate at least 10 million models for global calculation. By, adopting NSGA-II an appropriate Pareto front could be got by calculating less than 10 thousand models. However, calculating all the cases in the progress of the optimization based on NSGA-II still has a large computation cost. Therefore, the

Kriging model is chosen to construct the approximate multi-objective optimization models.

The Pareto front got by NSGA-II in level 1 optimization is shown in Fig.12. All the 5000 cases calculated in the iterations are shown in the figure. The blue points are the non-dominated solutions, the green points are the cases which are dominated by other cases, and the yellow cases are the cases that do not meet the constraints.

For further optimization, three candidate points are chosen from the Pareto front of level 1 in this research which are listed in Table VI. When choosing the candidate points for further optimization there are no clear guidelines. However, it is recommended that the chosen candidates should keep a distance from each other to make the next optimization level can cover a broader Pareto front.

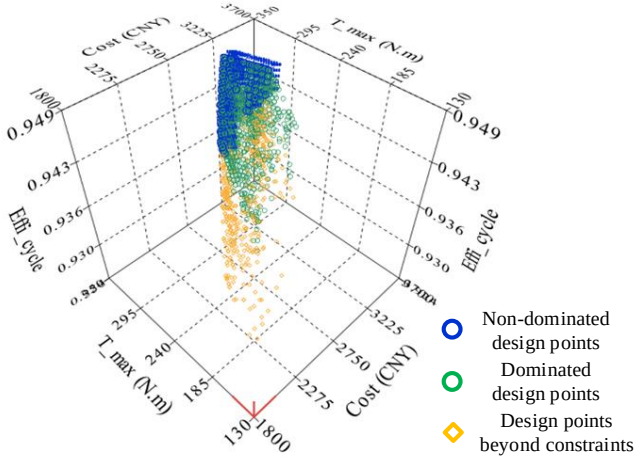

Fig. 12. Optimization results of the level 1 optimization.

D. Optimization Results and Computation Cost

In level 2 optimization, three candidates will be optimized independently and the combined optimization results of the three candidates are shown in Fig.13(a). As the point on one Pareto front may be dominated by another point get from another Pareto front the Pareto front of level 2 needs to combine the optimization results get from all three candidates, as shown in Fig.13(b).

After level 2 optimization, point 2-1 is chosen for further optimization in level three. The parameters of points 2-1 are given in Table VII.

Table VI.
Candidate Points of the Level 1 Optimization

Parameters	Initial	Point 1-1	Point 1-2	Point 1-3
k_1 (mm)	0.7	0.69	0.62	0.71
W_{coil} (mm)	7.9	8	7.6	7.9
h_{PM} (mm)	11.8	10.2	12.8	10
Cost (CNY)	3256	2700	3350	2538
T_{max} (N·m)	*285*	272	320	253
$Effi_{cycle}$%	*93.8*	94.6	93.9	94.6
T_{rip}%	*3.9*	3.6	4.1	3.9

Table VII.
Optimization Results of the Second and Third Optimization Levels.

Vars.	Point 2-1 (RSM-optimized)	Point 2-1 (Quasi-3D-FEM)	Point 2-1 (3D-FEM)	Point -3 (3D-FEM)
k_1	0.69	0.69	0.69	0.69
W_{coil} (mm)	8.00	8.00	8.00	8.00
h_{PM} (mm)	10.2	10.2	10.2	10.2
k_{PM}	0.49	0.49	0.49	0.49
k_{PM1}	0.25	0.25	0.25	0.25
k_{PM2}	0.36	0.36	0.36	0.36
Lip_{in}(mm)	0	0	0	1.47
Lip_{out}(mm)	0	0	0	1.36
Cost (CNY)	2797	2797	2797	2965
T_{max} (N·m)	284.8	281.7	265.6	277.5
$Effi_{cycle}$%	94.51	94.47	94.45	94.42
T_{rip}%	3.21	3.19	3.33	3.25
$T_{demgloss}$‰	5.70	5.60	5.45	5.46

It should be noted that in the first two levels of optimization, the Quasi-3D-FEM model and the Kriging RSM model are adopted to reduce the calculation amount of the optimization. Therefore, the 3D-FEM model is used to calculate the performance of points 2-1 to verify the accuracy of the Quasi-3D-FEM and Kriging RSM model. As shown in Table VII, compared with the performance calculated by the 3D-FEM the efficiency, torque ripple, and high-temperature demagnetization torque loss are the performance get from the Quasi-3D-FEM model and Kriging RSM model only have a small error. The error of maximum torque is relatively high which is due to the ignore the end effect and the RSM model value is based on the results of 3D-FEM models. However, optimization is to study the trend of performance, and such error is acceptable.

Point 2-1 is chosen for further optimization in level 3 and the Pareto front of level 3 is shown in Fig.14. Point 3 is finally chosen as the optimized result of this study which specific parameters and performance listed in Table VII. Compared with the initial value in Table VI, this optimization enhances the efficiency by 0.6%, reduces the cost by 9%, and sacrifices the maximum torque by only 2.6% which still meets the design requirements.

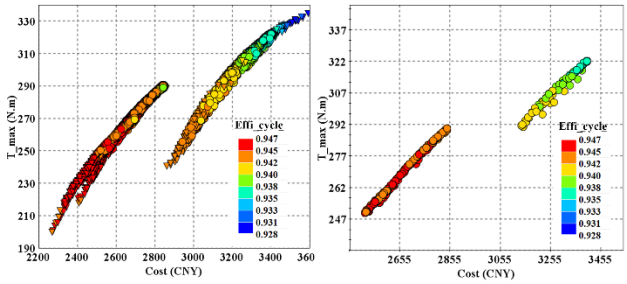

(a) (b)

Fig. 13. Optimization results of the optimization level 2. (a) Optimization results of three candidates, (b) Combined Pareto front of optimization level 2.

Table V.
Parameters to be Optimized and Objectives of Different Optimization Levels.

Level	Opt. Inputs	Var.	Model	Objectives	Constraint	Outputs	Models for RSM	Populations ×terations
Level 1	Initial design/ Parameters range	k_1 W_{coil}, h_{PM}	Quasi-3D FEM	T_{max}, $Cost$, $Effi_{cycle}$%	$Cost$<3400, T_{rip}%<6%, T_{max}>250N·m, $Effi_{cycle}$%>92%	Point 1-1 Point 1-2 Point 1-3	200	100×50
Level 2	Point 1-1, Point 1-2, Point 1-3	k_{PM} k_{PM1} k_{PM2}	Quasi-3D FEM	$Cost$, T_{max}, $Effi_{cycle}$%	$Cost$<3400, T_{rip}%<6%, $T_{demgloss}$‰<6‰	Point 2-1	200	100×50
Level 3	Point 2-1	Lip_{in} Lip_{out}	3D FEM	$Cost$, T_{max}	NA	Result	100	100×20

In the aspect of computation cost, compared to 3D FEM need 300000 nodes Quasi-3D FEM model only needs 60000 nodes which can save the computation time by 80%. By adopting a multilevel strategy, the number of models that need to be calculated can be saved by over 60%. Further, using the Kriging RSM model can support the one optimization level with only 200 FEMs, while optimization fully depended on FEMs needing over 3000 models to realize effective convergence. In general, the Quasi-3D FEM, multilevel strategy, and Kriging RSM model adopted in this study have greatly improved the efficiency of optimization progress.

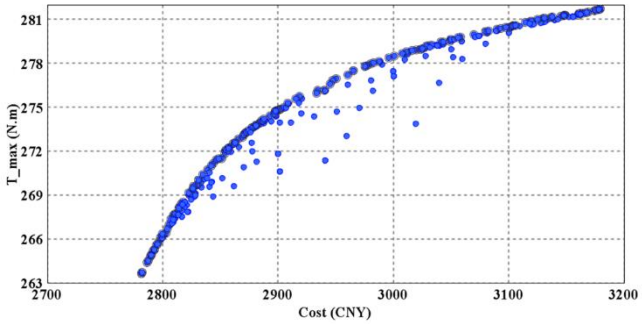

Fig. 14. Optimization results of optimization level 3.

IV. EXPERIMENTS

According to the optimization results, the AFPMSM is manufactured for experimental validation. The prototype machines are shown in Fig. 15. The experimental platform is shown in Fig. 16, where an electric vehicle machine test platform is used to test the performance of the AFPMSM prototype. As shown in Fig.16(a), a driving machine is connected to a grinding wheel and the prototype is installed in a wheel. In the no-load test, by applying a vertical load to the AFPMSM prototype, the grinding wheel can drag the machine to rotate. The tested no-load phase back-EMF waveform at 400 r/min is shown in Fig.17(a), and Fig.17(b). compares the FEA-predicted and measured no-load phase back-EMF waveforms at 400 r/min. As shown, it is evident that the proposed AFPMSM has sinusoidal and symmetric back-EMFs, the error between the test and FEA is less than 5%.

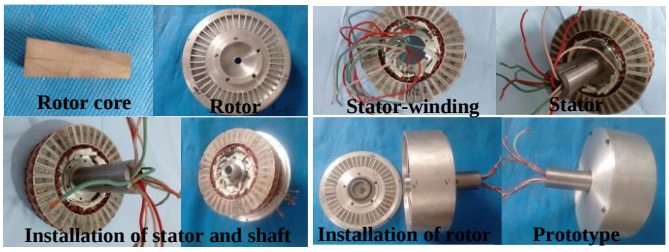

Fig. 15. A prototype of IPMSM.

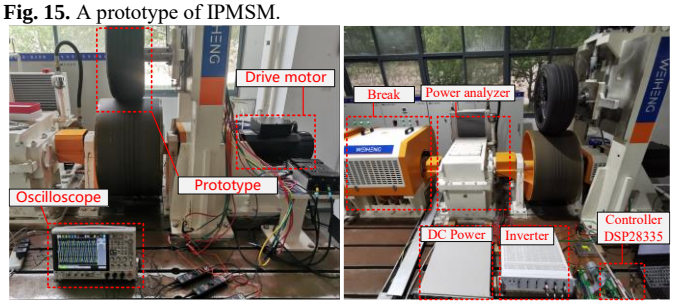

Fig. 16. Wheel hub machine experimental platform. (a)No-load test experiment platform, (b) Load test platform.

Fig. 16(b) shows the load test platform of the AFPMSM prototype which consists of a break, a power analyzer, DC power, an inverter, and a controller based on DSP28335. As the prototype and load are not rigidly connected, an accurate torque waveform cannot be tested. Therefore, fixed load torque is provided by the grinding wheel, and the load current is tested as shown in Fig.18. As shown in Fig.18. in low load conditions (<180 Nm) the error of current is less than 5%, and the error gets larger with the increase of load torque. The error is relatively large, but considering that the test method used is the indirect test, many factors cause the error, including transmission radius measurement error, transmission structure torque loss, and relative slip, especially under high load.

Fig.19 shows the Torque and power test external characteristic curve of the prototype. The test is under the condition of DC Voltage 300V, inverter current 75 A, and control strategy MTPA and magnetic field weakening control. As shown, the prototype can maintain maximum torque in the speed range of 0-550 r/min. when the speed is over 550 r/min, the DC voltage is not enough to keep MTPA control the prototype switch to magnetic field weakening control. At the

speed of 800r/min, the prototype reaches a maximum power of 15kW. The speed of the prototype can reach 1200r/min and keep a torque over 90 Nm.

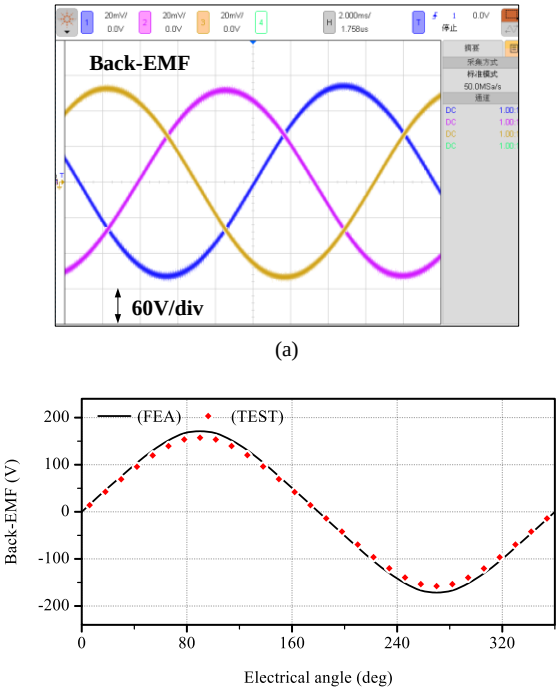

Fig. 17. AFPMSM no-load Back-EMF. (a) Test Back-EMF (b) Comparison of Test and FEA Back-EMF.

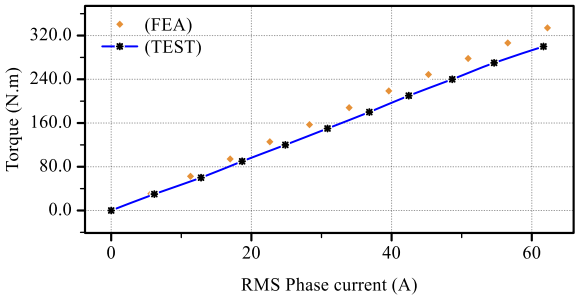

Fig. 18. RMS Phase current under different torque loads.

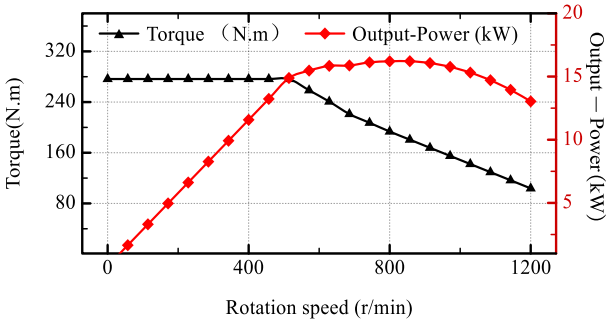

Fig. 19. Torque and power test external characteristic curve of the prototype.

Fig. 20 (b). shows the tested efficiency map of the prototype under MTPA and flux weakening control strategy. The proposed machine can reach the maximum torque of 280 Nm and keep constant torque over 500 r/min. The efficiency of the main operation ranges in the drive cycle is over 92%. Compare with the efficiency map calculated by FEA as shown in Fig. 20 (a) the maximum is 5% lower which is due to the deviation of flux linkage and consistent with the back-EMF results. and the efficiency is about 0.5% lower than the FEA value which is due to some losses such as bearing loss and wind loss are ignored in FEA. Overall, the proposed AFPMSM matches the design requirements well.

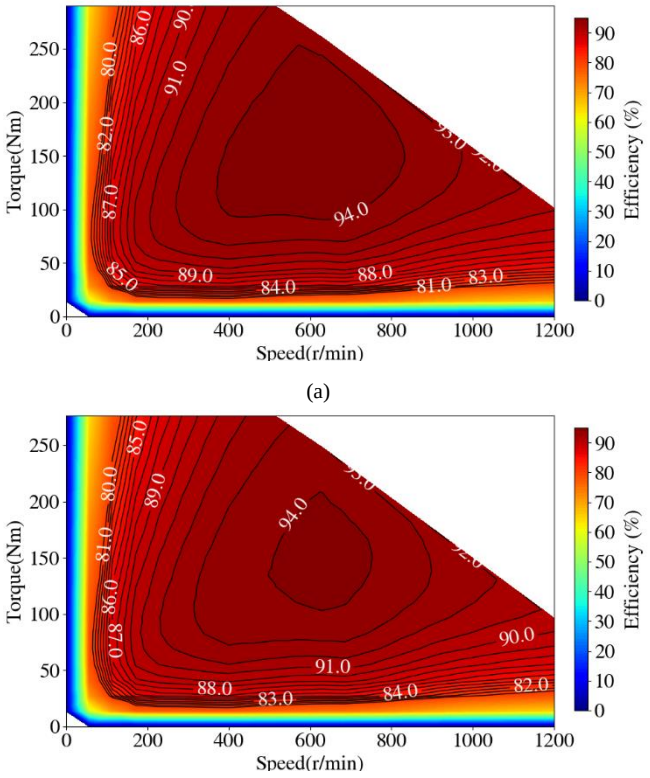

Fig. 20. Efficiency map (a) FEA, (b) Tested.

V. Conclusion

In this paper, a spoke-type AFPMSM for in-wheel drive operation and its multi-objective optimization was carried out. Firstly, different topologies of AFPSMS are compared and a spoke-type AFPMSM with a trapezoidal permanent magnet was proposed considering the requirements and constraints of in-wheel drive application. Then, the initial design is obtained according to the working points during the driving cycle and power dimension equations. The basic performance including magnetic density, cogging torque, Back-EMF, load torque, and demagnetization of the initial design are also calculated in section II. Secondly, multi-objective optimization based on a multilevel strategy is carried out in which multilevel strategy, Quasi-3D FEM model, and Kriging model are adopted to enhance the efficiency of the optimization progress. The proposed optimization method has achieved good optimization results and saved a lot of calculation time. Finally, a prototype is manufactured for experimental validation. The no-load and load performance of the prototype is consistent with the calculation results. Besides, the prototype has good flux weakening which is applicable for in-wheel drive applications.

The novel structure of spoke type-AFPMSMs for EV application provides a new electromagnetic structure solution for wheel drive applications. The optimization method proposed in this paper can reduce the computation time cost in the optimization work for other axial flux machines.

REFERENCES

[1] X. Sun, Y. Zhang, Y. Cai, and X. Tian, "Compensated deadbeat predictive current control considering disturbance and VSI nonlinearity for in-wheel PMSMs," *IEEE/ASME Trans. Mechatronics*, vol. 27, no. 5, pp. 3536-3547, Oct. 2022.

[2] H. Chen, X. Liu, N. A. O. Demerdash, A. M. E.-. Refaie, J. Zhao, and J. He, "Comparison and design optimization of a Five-Phase Flux-Switching PM machine for In-wheel traction applications," *IEEE Transactions on Energy Conversion,* vol. 34, no. 4, pp. 1805-1817, 2019.

[3] X. Sun, T. Li, X. Tian, and J. Zhu, "Fault-tolerant operation of a six-phase permanent magnet synchronous hub motor based on model predictive current control with virtual voltage vectors," *IEEE Trans. Energy Convers.*, vol. 37, no. 1, pp. 337-346, Mar. 2022.

[4] C. H. T. Lee, W. Hua, T. Long, C. Jiang, and L. V. Iyer, "A critical review of emerging technologies for electric and hybrid vehicles," *IEEE Open Journal of Vehicular Technology,* vol. 2, pp. 471-485, 2021.

[5] X. Sun, Z. Shi, Y. Cai, G. Lei, Y. Guo, and J. Zhu, "Driving-cycle oriented design optimization of a permanent magnet hub motor drive system for a four-wheel-drive electric vehicle," *IEEE Trans. Transport. Electrific.*, vol. 6, no. 3, pp. 1115-1125, Sep. 2020.

[6] Z. Jin, X. Sun, G. Lei, Y. Guo, and J. Zhu, "Sliding mode direct torque control of SPMSMs based on a hybrid wolf optimization algorithm," *IEEE Trans. Ind. Electron.*, vol. 69, no. 5, pp. 4534-4544, May 2022.

[7] S. Amin, S. Khan, and S. S. H. Bukhari, "A comprehensive review on axial flux machines and its applications," in *2019 2nd International Conference on Computing, Mathematics and Engineering Technologies (iCoMET)*, 2019, pp. 1-7.

[8] X. Sun, Y. Zhang, G. Lei, Y. Guo, and J. Zhu, "An improved deadbeat predictive stator flux control with reduced-order disturbance observer for in-wheel PMSMs," *IEEE/ASME Trans. Mechatronics*, vol. 27, no. 2, pp. 690-700, Apr. 2022.

[9] X. Kong, Y. Hua, Z. Zhang, C. Wang, and Y. Liu, "Analytical modeling of high-torque-density spoke-type permanent magnet in-wheel motor accounting for rotor slot and eccentric magnetic pole," *IEEE Transactions on Transportation Electrification,* vol. 7, no. 4, pp. 2683-2693, 2021.

[10] B. Dianati, S. Kahourzade, and A. Mahmoudi, "Axial-flux induction motors for electric vehicles," in *2019 IEEE Vehicle Power and Propulsion Conference (VPPC)*, 2019, pp. 1-6.

[11] X. Wang, Y. Fan, C. Yang, Z. Wu, and C. H. T. Lee, "Multi-objective optimization framework of a radial-axial hybrid excitation machine for electric vehicles," *IEEE Transactions on Vehicular Technology*, pp. 1-10, 2022.

[12] R. Huang, Z. Song, H. Zhao, and C. Liu, "Overview of axial-flux machines and modeling methods," *IEEE Transactions on Transportation Electrification,* vol. 8, no. 2, pp. 2118-2132, 2022.

[13] D. K. Lim, Y. S. Cho, J. S. Ro, S. Y. Jung, and H. K. Jung, "Optimal design of an axial flux permanent magnet synchronous motor for the electric bicycle," *IEEE Transactions on Magnetics,* vol. 52, no. 3, pp. 1-4, 2016.

[14] J. Gillies, T. Lambert, A. Emadi, and B. Bilgin, "Axial-flux switched reluctance motor design for a light electric vehicle application," in *2022 IEEE Transportation Electrification Conference & Expo (ITEC)*, 2022, pp. 790-795.

[15] M. Muthusamy, J. Hendershot, and P. Pillay, "Design of a Spoke Type PMSM with SMC stator core for traction applications," *IEEE Transactions on Industry Applications,* pp. 1-18, 2022.

[16] J. Hou, W. Geng, Q. Li, and Z. Zhang, "3-D equivalent magnetic network modeling and fea verification of a novel axial-flux hybrid-excitation In-wheel motor," *IEEE Transactions on Magnetics,* vol. 57, no. 7, pp. 1-12, 2021.

[17] Y. Xu, Q. Wu, and Q. Gao, "Equivalent magnetic network of novel disk transverse-flux permanent magnet brushless machine based on soft magnetic composite material," in *2016 IEEE Conference on Electromagnetic Field Computation (CEFC)*, 2016, pp. 1-1.

[18] R. Alipour-Sarabi, Z. Nasiri-Gheidari, and H. Oraee, "Development of a three-dimensional magnetic equivalent circuit model for axial flux machines," *IEEE Transactions on Industrial Electronics,* vol. 67, no. 7, pp. 5758-5767, 2020.

[19] H. J. Park, H. K. Jung, S. Y. Jung, Y. H. Chae, and D. K. Woo, "Field reconstruction method in axial flux permanent magnet motor with overhang structure," *IEEE Transactions on Magnetics,* vol. 53, no. 6, pp. 1-4, 2017.

[20] B. Guo, Y. Huang, F. Peng, J. Dong, and Y. Li, "Analytical modeling of misalignment in axial flux permanent magnet machine," *IEEE Transactions on Industrial Electronics,* vol. 67, no. 6, pp. 4433-4443, 2020.

[21] X. Wang, Y. Fan, X. Lu, Q. Chen, and C. H. T. Lee, "Multiobjective optimization of a dual stator brushless hybrid excitation motor based on response surface model and NSGA 2," *IEEE Transactions on Industry Applications,* vol. 58, no. 5, pp. 6105-6114, 2022.

[22] X. Sun, N. Xu, and M. Yao, "Sequential subspace optimization design of a dual three-phase permanent magnet synchronous hub motor based on NSGA III," *IEEE Transactions on Transportation Electrification,* vol. 9, no. 1, pp. 622-630, Mar. 2023.

[23] K. Diao, X. Sun, G. Bramerdorfer, Y. Cai, G. Lei, and L. Chen, "Design optimization of switched reluctance machines for performance and reliability enhancements: A review," *Renew. Sustain. Energy Rev.*, vol. 168, no. 10, Art. no.: 112785, Oct. 2022.

[24] Z. Shi, X. Sun, G. Lei, X. Tian, Y. Guo, and J. Zhu, "Multiobjective optimization of a five-phase bearingless permanent magnet motor considering winding area," *IEEE/ASME Transactions on Mechatronics,* vol. 27, no. 5, pp. 2657-2666, 2022.

[25] G. Lei, T. Wang, J. Zhu, Y. Guo, and S. Wang, "System-level design optimization method for electrical drive systems—robust approach," *IEEE Transactions on Industrial Electronics,* vol. 62, no. 8, pp. 4702-4713, 2015.

[26] Z. Jin, X. Sun, L. Chen, and Z. Yang, "Robust multi-objective optimization of a 3-pole active magnetic bearing based on combined curves with climbing algorithm," *IEEE Trans. Ind. Electron.*, vol. 69, no. 6, pp. 5491-5501, Jun. 2022.

[27] A. Mahmoudi, S. Kahourzade, N. A. Rahim, and W. P. Hew, "Design, analysis, and prototyping of an axial-flux permanent magnet motor based on genetic algorithm and finite-element analysis," *IEEE Transactions on Magnetics,* vol. 49, no. 4, pp. 1479-1492, 2013.

[28] K. Deb, A. Pratap, S. Agarwal and T. Meyarivan, "A fast and elitist multiobjective genetic algorithm: NSGA-II," *IEEE Transactions on Evolutionary Computation*, vol. 6, no. 2, pp. 182-197l, 2002.

[29] S. Verma, M. Pant and V. Snasel, "A Comprehensive Review on NSGA-II for Multi-Objective Combinatorial Optimization Problems," *IEEE Access*, vol. 9, pp. 57757-57791, 2021.